The Effect of Sr-Doping on Structural, Optical, Catalytic, and Photocatalytic Properties of α-MnO₂ Nanowires Synthesized *via* a Hydrothermal Route

S. Mammeri[a],*, O. Halimi[a], M. Sebais[a], S. Touahri[a,b], B. Boudine[a], A. Azizi[c] and M.T. Soltani[d]

[a]*Laboratory of Crystallography, University Frères Mentouri-Constantine 1, Algeria*
[b]*University Larbi Ben M'hidi, Oum El Bouaghi 04000, Algeria*
[c]*Phase Transformation Laboratory, University Frères Mentouri-Constantine 1, Algeria*
[d]*University Mohamed Khider, Biskra 07000, Algeria*

Undoped and strontium (Sr)-doped α-manganese dioxide (MnO₂) nanowires were synthesized through a hydrothermal method to be used as catalysts and photocatalysts for the degradation of methylene blue (MB) dye. The Sr concentrations were 2, 4, 6, and 8 wt%. X-ray diffraction demonstrated the synthesis of the α-MnO₂ tetragonal phase with large tunnels along the c-axis which incorporated the Sr dopant. Fourier-transform infrared spectroscopy and Raman spectroscopy confirmed the synthesis of α-MnO₂. The SEM microscopy showed that α-MnO₂ crystallites had nanowire morphology with lengths up to 5.91 μm. Optical investigation revealed that the α-MnO₂ nanowires had a band gap that slightly decreased with increasing Sr concentration. In addition, the photoluminescence spectroscopy exhibited some emission bands in the visible region. The evaluation of catalytic and photocatalytic activities of α-MnO₂ nanowires was conducted against Sr concentration, and the results showed high efficiency in the catalytic removal of MB, which reached 49.93% for the undoped sample and almost 99.63% for the highly doped sample in only 2 min. Under UV irradiation ($\lambda = 365$ nm), the photocatalytic degradation by the undoped sample was higher and reached 97.74% in 60 min. The effect of UV irradiation, size, morphology, and Sr-doping of α-MnO₂ nanowires greatly improved the degradation of MB and led to its mineralization.

Keywords: Hydrothermal synthesis, Sr-doped α-MnO₂ nanowires, Structural and optical properties, Catalytic and photocatalytic activities, Methylene blue

INTRODUCTION

Nowadays, the discharges of daily human consumption as well as those of various industries cause considerable damage to the environment. Pollution of the soil and air by harmful substances, such as harmful gases and organic residues, can have serious repercussions for the lives of humans and animals; thus, it can be noted that environmental pollution is actually a serious challenge [1-3]. Appropriate and effective solutions to contain the damage caused and avoid hampering technological development, therefore, must

be quickly developed. Among the solutions proposed, the degradation of organic pollutants by heterogeneous photocatalysis has led to satisfactory results in several cases, where the degradation exceeded 95% [2]. The rate of degradation is related to some physicochemical properties of the catalyst, such as its chemical nature, crystallographic structure, concentration of doping, and the size and morphology of crystallites [1,4-5]. Metallic oxide semiconductors, such as TiO₂ [6], ZnO [7], and SnO₂ [5], have been shown to be efficient in the field of photocatalysis. In addition to the above semiconductors, manganese dioxide (MnO₂) has also been demonstrated to have high efficiency in the degradation of numerous organic pollutants

---

*Corresponding author. E-mail: sabahww82@gmail.com

[3,8,19,10]. MnO$_2$ can be found in different crystal structures (α, β, γ, and δ) that have phase-specific properties [11]. Moreover, it is obvious that nanostructured materials exhibit enhanced activities due to their large surface area and size effects [12]. Some studies have reported that manganese oxides are promising candidates for use in the cleanup of wastewater and the degradation of dyes in different surroundings [9]. With their low cost, availability, and excellent photoactivity, manganese oxide materials have attracted great interest [10]. Doping, by inserting ions or molecules into the crystal lattice of materials, often significantly modifies the physicochemical properties of materials; the evolution of these properties depends on the nature and concentration of the dopant. Studies on catalytic and photocatalytic properties of different phases of MnO$_2$ are available in the literature, but to the best of our knowledge, no study has yet investigated the performance of Sr (strontium)-doped α-MnO$_2$ nanowires (NWs). This paper presents the results of an investigation on the effects of Sr-doping on structural, morphological, optical, and, particularly, catalytic and photocatalytic properties of undoped and Sr-doped α-MnO$_2$ NWs synthesized by a hydrothermal method. The insertion of different concentrations (2, 4, 6, and 8 wt%) of Sr^{2+} ions into the α-MnO$_2$ lattice had a favorable effect on the size and the specific surface area (SSA) of the NWs and promoted the creation of new active sites on the surface of NWs, which are essential for efficient catalytic and photocatalytic activities. A significant improvement was observed in the catalytic activity of Sr-doped against undoped α-MnO$_2$ in the removal of the organic pollutant methylene blue (MB). The total degradation of MB was reached in a very short time.

EXPERIMENTAL

Hydrothermal Synthesis of Undoped and Sr-Doped α-MnO$_2$ NWs

The undoped and Sr-doped α-MnO$_2$ NWs were prepared using a hydrothermal reaction according to the previously reported protocol [9-10,13]. In a typical synthesis, a mixture of 0.2766 g of potassium permanganate (KMnO$_4$), 0.4463 g of hydrated manganese sulfate (MnSO$_4$.H$_2$O), and strontium chloride hexahydrate (SrCl$_2$.6H$_2$O) were used as doping sources. The chemical reactants were added to 140 ml of

deionized water. After magnetic stirring and heating at 50 °C for 1 h, a homogeneous solution was obtained and then transferred into a Teflon-lined stainless-steel autoclave (capacity 160 ml). The autoclave was sealed and heated in an oven at 90 °C for 24 h. When the thermal treatment was completed, the autoclave was cooled down to room temperature naturally. The reactions involved during the hydrothermal processes can be briefly described as follows [14]:

$$2KMnO_4 + 3MnSO_4 + 2H_2O \rightarrow 5MnO_2(\alpha type) +$$
$$K_2SO_4 + 2H_2SO_4 \qquad\qquad (1)$$
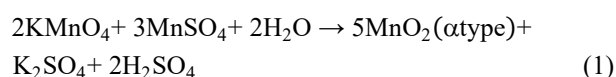
The obtained brown powders were washed several times with deionized water and absolute ethanol to remove impurities and finally dried at 75 °C for 10 h. The used Sr-doping concentrations were 0, 2, 4, 6, and 8 wt%, and the corresponding samples were respectively named MnSr0, MnSr2, MnSr4, MnSr6, and MnSr8. These powders were characterized by different techniques to check their structural, morphological, optical, catalytic, and photocatalytic properties.

Structural and Optical Characterization Methods

The structure of synthesized α-MnO$_2$ NPs was analyzed by X-ray diffraction patterns performed on a PANalytical X'Pert PRO diffractometer in 2θ range of 08°-80º using the CuKα radiation (λ = 1.5406 Å) with an accelerating voltage of 45 KV and an applied current of 40 mA. The Raman spectroscopy was carried out using a Horiba LabRam HR Evolution spectrometer and an excitation wavelength of 473 nm. The Fourier-transform infrared spectroscopy (FT-IR) was performed on a Thermo Fisher Nicolet 6700 spectrometer. The morphology of NWs was analyzed with a JSM-7100 field emission scanning electron microscope (SEM). The optical absorbance spectra of the prepared samples were recorded in the UV-Vis range using a UV-750 JASCO spectrophotometer, and the photoluminescence (PL) spectra were collected with a Yvon Horiba FluoroMax-4P fluorometer using a xenon flash lamp (150 W) at an excitation wavelength of 350 nm and room temperature with a 3 nm aperture for the excitation source and the emission detector.

Catalytic and Photocatalytic Procedure

Catalytic and photocatalytic activities of the undoped and Sr-doped α-MnO$_2$ powders were evaluated using an aqueous solution of MB. An amount of 0.25 g of the catalyst was added to 50 ml of MB dye solution (6 mg l^{-1}). Then, the mixture was magnetically stirred in the dark to achieve adsorption/desorption equilibrium. To check this equilibrium, 5 ml of the solution was withdrawn after different time intervals and centrifuged to obtain the catalyst. To evaluate the adsorption effect, the variation in the initial concentration of MB in the solution was estimated by UV-Vis absorbance spectra using a JASCO V-750 UV-Vis spectrophotometer with a quartz cell (3 ml). To evaluate the photocatalytic effect, after adsorption/desorption equilibrium, which was reached after 18 min in the dark, the solution (MB + catalyst) maintained under stirring was submitted to a UV light source (VL-215. LC, 15 W, and 365 nm) placed at 10 cm above the irradiated surface, which was 63.62 cm^2. The variation in the concentration of MB was analyzed after several irradiation times. The degradation of MB was determined using Eq. (2) [4].

$$\text{Degradation efficiency (\%)} = \left[\frac{C_0 - C_t}{C_0}\right] \times 100 \qquad (2)$$

where C0 is the initial concentration and Ct is the concentration after a time t.

RESULTS AND DISCUSSION

Structural and Morphological Properties

X-ray diffraction analysis. The crystallographic structure of as-synthesized NWs of undoped and Sr-doped MnO$_2$ obtained from XRD patterns is shown in Fig. 1. According to the JCPDS file 44-0141, all reflections could be indexed to the structure of α-MnO$_2$, which had the symmetry of a tetragonal space group I4/m and the cell parameters of a = b = 9.7847 Å and c = 2.8630 Å [10,14]. Moreover, according to the JCPDS File 44-0140, the obtained XRD patterns could also be attributed to the compound α-MnO$_2$(0.3H$_2$O), which showed crystallographic characteristics.

No peaks were observed for Sr metal compounds or residual phases. This suggests that the incorporation of Sr^{2+} ions into the wide tunnels of α-MnO$_2$ lattice was done
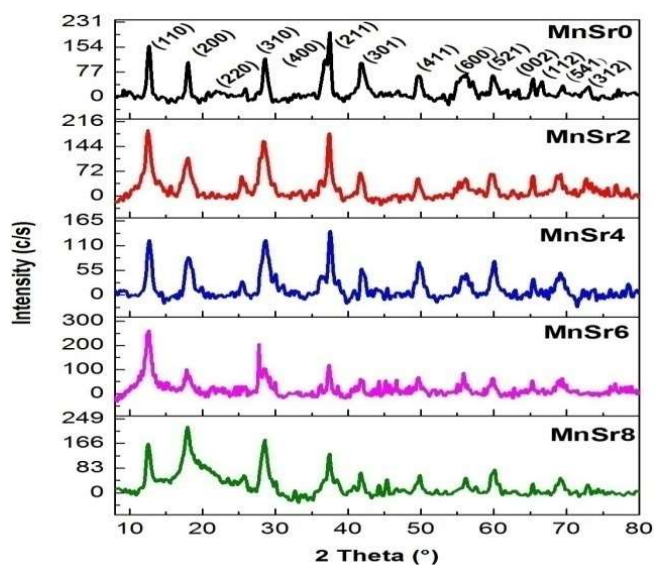

Fig. 1. XRD patterns of undoped and Sr-doped α-MnO$_2$ NWs.
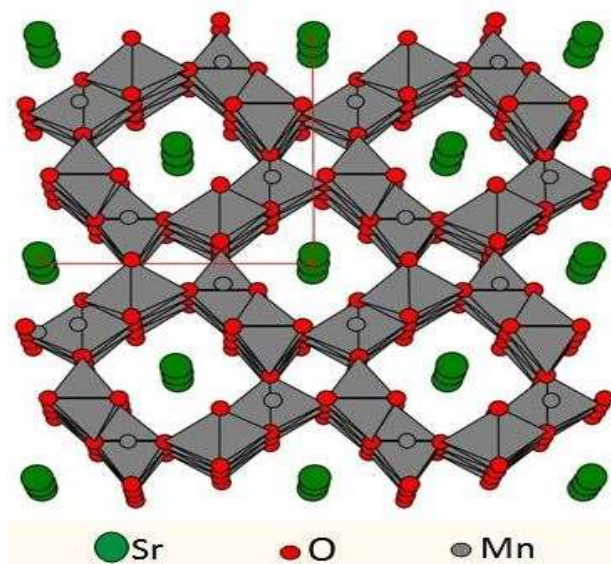

Fig. 2. The crystal structure of α-MnO$_2$ with both (2×2) and (1×1) tunnels along the c-axis.

successfully, as shown in Fig. 2. The H$_2$O molecules can also be housed in these tunnels [15].

The effect of Sr-doping on the α-MnO$_2$ structure was studied by determining the variation in lattice parameters (a and c) for undoped and Sr-doped samples (Table 1) using the following Eqs. ((3) and (4)) [4]:

$$2d_{hkl} \sin\theta = n\lambda \qquad (3)$$

$$\frac{1}{d_{hkl}^2} = \frac{h^2 + k^2}{a^2} + \frac{l^2}{c^2} \qquad (4)$$

Table 1 shows that the lattice parameter along the c-axis was almost constant, but in the plane (a,b) perpendicular to the c-axis, the lattice parameters a (b) presented weak divergences, which were caused by distortions due to the non-stoichiometry of the lattice induced by the incorporation of Sr^{2+} ions [16-17]. Thus, it can be said that there were no significant variations in the lattice parameters (a and c), which confirms the insertion of Sr^{2+} ions ($RSr^{2+} = 1.26$ Å) in wider tunnels 2×2 (4.6 Å × 4.6 Å) along the c-axis of tetragonal α-MnO_2 [18].

Based on XRD spectra (Fig. 1), when Sr concentration increases, a decrease was observed in the peak intensity related to the most intense peak corresponding to the plane (211), which could be explained by the fact that the highest concentrations of Sr-doping (6 and 8 wt%) caused more pressure and disorder inside the crystal lattice of α-MnO_2. The tunnel structure of α-MnO_2 allows it to be used as a photocatalyst because the photocatalytic process is a redox process involving electron transfer and associated cation to maintain the electrical neutrality equilibrium [18].

The mean crystallite D(hkl) sizes corresponding to the diffraction planes (110), (200), and (002) were calculated using the following Scherrer's equation (5) and are presented in Table 2 [4]:

$$D_{(hkl)} = \frac{0.9\lambda}{\beta\ co} \qquad (5)$$

The obtained values corresponded to the nanometric scale. The value of D(002) expressed the average size of the cross-section along the c-axis and was larger in samples with greater Sr-doping concentrations.

Morphology and Size Analysis

The morphology and size of as-synthesized α-MnO_2 NWs were also analyzed using a field emission scanning electron microscope (SEM). Figures 3a, b, c and d display the SEM images of the undoped and Sr-doped α-MnO_2 NWs (scale 100 nm). For all samples, the one-dimensional (1D) morphology of NWs can be clearly observed. The same

Table 1. Lattice Parameters (a, c) of Undoped and Sr-Doped α-MnO_2 NWs

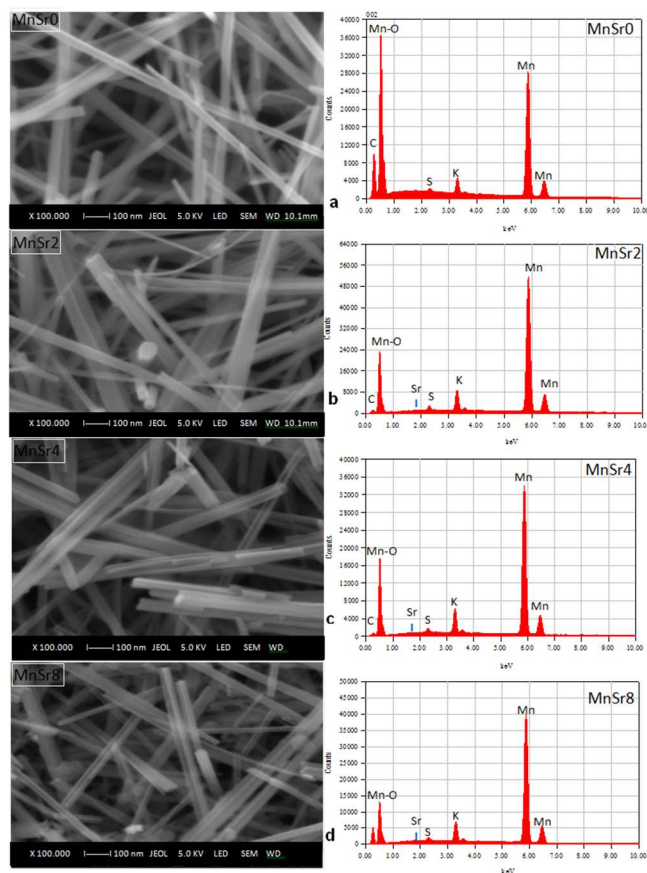| Sample	Diffraction plane (200)		Diffraction plane (002)	
	2θ	a = b	2θ	c
	(°)	(Å)	(°)	(Å)
MnSr0	18.085	9.802	65.400	2.852
MnSr2	18.026	9.834	65.413	2.851
MnSr4	18.101	9.794	65.452	2.849
MnSr6	17.993	9.852	65.347	2.853
MnSr8	18.058	9.817	65.394	2.852

Fig. 3. SEM images and energy-dispersive x-ray spectroscopy (EDX) spectra of undoped and Sr-doped α-MnO_2 NWs.

morphology was earlier reported for α-MnO_2 NWs in the literature [2,11].

Table 2. The Average Sizes of α-MnO$_2$ Crystallites Estimated by Scherrer's Equation Along the [002], [200], and [110] Axes

Sample	Scherrer's sizes D$_{(hkl)}$ of crystallites					
	Plane (110)		Plane (200)		Plane (002)	
	2θ	D	2θ	D	2θ	D
	(°)	(nm)	(°)	(nm)	(°)	(nm)
MnSr0	12.680	13.95	18.085	14.86	65.405	21.23
MnSr2	12.576	07.76	17.998	06.59	65.414	21.24
MnSr4	12.729	09.94	18.174	07.83	65.483	22.08
MnSr6	12.578	08.21	17.989	09.90	65.348	32.16
MnSr8	12.609	13.33	17.993	11.26	65.394	27.61

Table 3. Dimensions of α-MnO$_2$ NWs, Measured from SEM Images, and the Average Surface of Particles

Sample	Lengths (μm)	Cross-section edges (nm)	Particle average surface area (SA) (μm^2)	Surface area ratio
	Average (μm)	Average (nm)		
MnSr0	1.03 to 5.91	10.01 to 63.65	0.51	$\frac{0.51}{0.51} = 1$
	3.47	36.83		
MnSr2	0.83 to 3.11	10.16 to 65.67	0.30	$\frac{0.51}{0.30} = 1{,}70$
	1.97	37.91		
MnSr4	0.74 to 2.22	10.20 to 65.72	0.22	$\frac{0.51}{0.22} = 2{,}31$
	1.48	37.96		
MnSr8	0.28 to 2.17	10.32 to 65.79	0.18	$\frac{0.51}{0.18} = 2{,}83$
	1.22	38.05		

The as-synthesized α-MnO$_2$ NWs had various dimensions (Table 3) and were characterized by their lengths, which reached 5.91 μm, and nanometric cross sections, the sizes of which reached 65.79 nm. This observation indicates the single-crystalline nature of undoped and Sr-doped α-MnO$_2$ NWs. Furthermore, these NWs were transparent and smooth, confirming their high quality. From Fig. 3a, it can be seen that the undoped α-MnO$_2$ NWs had a morphology with a square cross-section, the edge length of which was not constant. For the Sr-doped α-MnO$_2$ samples (Figs. 3b-d), while the particles had the same 1D morphology, they showed some variations in the dimensions. Overall, the length decreased while the cross-section edge increased

slightly when the Sr concentration increased (Table 3).

The values of crystallite sizes (cross-section) measured from SEM images were consistent with that calculated from XRD data using Scherrer's equation [16]. Moreover, from Table 3, it can be seen that the Sr-doping had a stronger effect on the length than the cross-section edge; however, the relatively long length of particles prevented their aggregation, which, in turn, increased the contact surface between α-MnO$_2$ NWs and MB solution and thus promoted both catalytic and photocatalytic activities.

The analysis by EDX of the chemical composition of the synthesized samples (Fig. 3) demonstrated the incorporation of Sr dopant into the α-MnO$_2$ lattice. The obtained results

Table 4. Effective Percentage of Sr Atoms in Synthesized α-MnO$_2$ NWs

Sample	Sr Percent (atom %)
MnSr0	0.00
MnSr2	0.05
MnSr4	0.24
MnSr8	0.55

(Table 4) revealed an increase in the number of Sr atoms with the increase in the doping concentration and confirmed the non-stoichiometry of the Sr-doped α-MnO$_2$ lattice. This non-stoichiometry could have potentially enhanced the catalytic activity of samples.

A Comparison of the SSA of the α-MnO$_2$ NWs

The SSA is an important characteristic of NWs. It expresses the total surface area of the particles per unit of mass and is particularly significant in the study of adsorption properties, heterogeneous catalysis, and reactions on particle surfaces. A larger SSA can provide more contact surface between the pollutant molecules in a solution and the catalyst particles, thus increasing the number of active sites during the catalytic and photocatalytic processes. Some experimental and theoretical methods are used to estimate the SSA of nanomaterials [19-22], but they often lead to discrepant results owing to the limitations of each method, such as flawed underlying theoretical assumptions and experimental artifacts arising from the handling and preparation of samples.

In this work, only the variations in the SSA, as a function of different concentrations of Sr-doping, were examined. In the case of the tetragonal morphology, by considering the average particle sizes of α-MnO2 NWs measured from SEM images (Table 3) and assuming a homogeneous size distribution, the surface area of one particle (SA) was calculated by Eq. (6):

$$SA = 2Da^2 + 4DaDc \tag{6}$$

where Da and Dc are the edge of the cross-section and the length of the α-MnO$_2$ NWs, respectively.

It is worthy of note that the SA (Table 3) decreased when the Sr concentration increased. The SA of one particle of the MnSr8 sample was 2.83 times smaller than that of one particle of the undoped sample. Therefore, for the same unit mass of samples, the number of particles was higher in the MnSr8 sample than in the undoped sample, allowing us to conclude that the SSA also had the same trend because it was also associated with the number of particles in the sample. It was observed that doping procured more active sites by increasing the SSA and thus improved the catalytic and photocatalytic activities of synthesized α-MnO$_2$ NWs.

Raman spectroscopy analysis. The changes in the lattice vibration properties caused by the insertion of Sr^{2+} ions in the tunnels of α-MnO$_2$ were analyzed by Raman spectroscopy. Generally, manganese oxide α-MnO$_2$ crystallizes in a tetragonal structure with the space group of I4/m, the symmetry of which allows the following active Raman vibration modes: 6Ag + 6Bg + 3Eg [23]. The apparition and intensity of Raman bands corresponding to these modes are related to several factors such as the morphology and size of the crystallites as well as the nature and concentration of the doping elements [1-2,4,13]. As can be seen, the Raman spectra of the elaborated NWs (Fig. 4) had an intense band located in a high-frequency shoulder at 634 cm^{-1}. This band corresponds to the Ag mode relative to the symmetric stretching vibration of the Mn-O bond in the MnO6 octahedra of the tetragonal structure of α-MnO$_2$ [23], and its strong intensity indicates the well-developed structure of α-MnO$_2$ with (2×2) type tunnels [24]. The intensity of this Ag mode decreases with increasing concentration of doping by Sr^{2+} ions as these ions occupy the tunnels (2×2) of the structure of α-MnO$_2$ (Fig. 2) and interfere with the vibrations of the Mn-O bonds of the MnO$_6$ octahedra [25]. Moreover, the position of this band slightly shifted towards the short wave numbers because the occupied (2×2) tunnels were sufficiently wide, so the Sr^{2+} ions could only cause small distortions even for relatively high concentrations. On the other hand, the reduction in the scattering intensity, particularly in the Ag symmetric mode, can be attributed to the breakdown of long-range translational crystal symmetry caused by the formation of defects owing to doping [26]. The SEM images confirm this suggestion (Fig. 3). A second band with low intensity was observed at around 342 cm^{-1}; it can be ascribed to the deformation mode of Mn-O-Mn [27]. The weak peak

observed at 532 cm^{-1} is due to the confinement of phonons by crystal defects and local distortions of lattice owing to the Sr-doping [28]. Another vibration band visible at about 816 cm^{-1} belong to the overtones of modes attributed to the α-MnO$_2$ phase [29]. Finally, it is worth noting that not all the active Raman bands appearing in the spectra had been reported by previous works in the literature devoted to the compound α-MnO$_2$ [23,26,28]. The difference in the results can be attributed to the variation in sizes and morphologies of particles, the doping elements, and synthesis protocols.

FT-IR analysis. The FT-IR spectra of the undoped and Sr-doped α-MnO$_2$ NWs are shown in Fig. 5. By comparing these spectra with those presented in the literature, it can be stated that the bands observed at 467 and 521 cm^{-1} correspond to the characteristic vibrations of Mn-O bond [30]. A weak band is visible at 619 cm^{-1}, which was previously reported to be associated with α-MnO2 materials [13]. The band located at 717 cm^{-1} can be attributed to the stretching mode of MnO$_6$ octahedra along the double-chain in manganese oxides with a tunnel structure similar to that of the α-MnO$_2$ group [30]. The band situated at 1125 cm^{-1} can be assigned to the vibration of hydroxyl groups. It can be seen that under the hydrothermal conditions, the symmetrical structures of MnO$_2$ oxides with the (2×2) and (1×1) tunnels were more stable than the less symmetrical structures with the (2×1) tunnels [11]. Furthermore, the water molecules or cations such as Sr^{2+} that were introduced into the tunnels of MnO$_2$ symmetrical structures during the synthesis helped to build and stabilize the structures [13]. Also, it has been reported that as in hydrous MnO2 samples, the vibration bands due to the interaction between Mn and surrounding species incorporated in the tunnels appeared at around 1620 and 1270 cm^{-1} [13]. The band that appeared at 1400 cm^{-1} can be attributed to the vibration mode of the Mn-O-Mn bonding in the α-MnO$_2$ phase [24] while the vibration at 1320 cm^{-1} was associated with the O-H bending vibrations connected with Mn atoms [31]. The presence of water molecules and Sr^{2+} cations in the wide tunnels of α-MnO$_2$ structure led to a small deformation of MnO$_6$ octahedra, which is expressed by the slight shift toward high frequencies bands in the FT-IR spectra (Fig. 5). It can be seen that the shift increased with the increase in the Sr-doping concentration. This observation is supported by the XRD results, which showed that the lattice parameters varied very little. Likewise, the intensity of
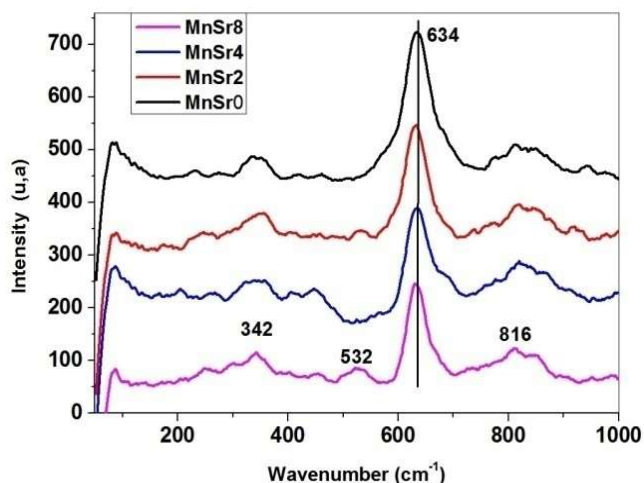

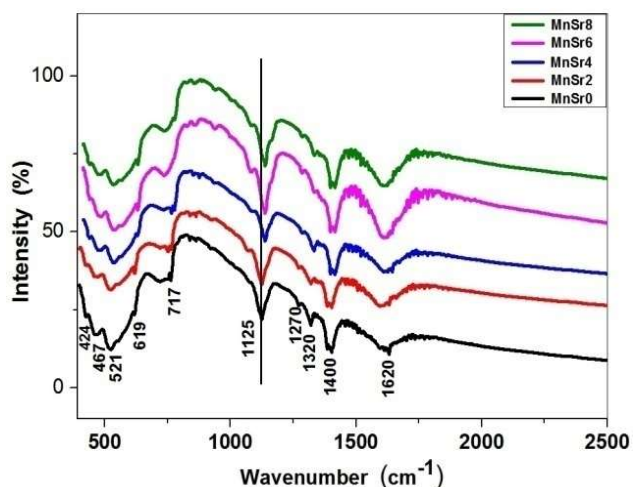**Fig. 4.** Raman spectra of undoped and Sr-doped α-MnO$_2$ NWs.

Fig. 5. FT-IR spectra of undoped and Sr-doped α-MnO$_2$ NWs.

bands related to vibrations of the Mn-O bond decreased with the presence of heavy Sr^{2+} cations, which, in turn, reduced the lattice vibrations. It has been demonstrated that the position and intensity of FT-IR bands are influenced by the nature and concentration of incorporated species in the tunnels of MnO$_2$ structures [13,32]. The O-H vibrations observed in FT-IR spectra suggest the presence of adsorbed water molecules inside the MnO$_2$ structure. This suggestion is supported by the XRD patterns of synthesized samples that can be related to the compound α-MnO$_2$(0.3H$_2$O). The

hydrating properties of MnO_2 may improve the cation diffusion to the surface of particles [31], thus increasing the catalytic activity.

Optical Properties

UV-Vis spectroscopy. The electronic properties of undoped and Sr-doped α-MnO_2 NWs were analyzed to evaluate the effect of doping on their optical absorption and band gap energy, which are involved in the photocatalytic process. Different band gap energy values have previously been reported for α-MnO_2 nanomaterials; these values vary in the range of 1.32-4.1 eV depending on the size, morphology, and doping of the samples [33-34].

Optical absorption spectra of undoped and Sr-doped α-MnO_2 NWs recorded in the UV-Vis ranged from 200 to 800 nm (Fig. 6). All samples exhibited a wide and weak absorption band that extended on all visible regions, mainly originating from the d-d transition of Mn^{4+} ions [33-34]. Also, a shoulder was visible at around 374 nm and a strong absorption below 250 nm, which could mainly have appeared due to the electron transition from the valence band to the conduction band [33-34]. From the spectra (Fig. 6), it can be observed that the tails of the absorption increased with the increase in the Sr-doping concentration; this effect can be ascribed to the generation of additional energy states within the band gap, which, in turn, extended the valence and conduction band edges. The formation of such defect states in the band gap led to a reduction in the recombination rate of photo-generated electron-hole pairs because, as reported in reference [1], charge transitions occur often through defects. For the Sr-doped α-MnO_2 samples, the spectra displayed a very slight shift toward the higher wavelengths for the absorption edge. This shift reflects a decrease in their band gap energy, which is a favorable characteristic for the photocatalytic activity.

For the synthesized α-MnO_2 NWs, the absorption coefficient F(R) was extracted from the reflectance spectra using the Kubelka-Munk Eq. (7) [1]:

$$F(R) = \frac{(1-R)^2}{2R} \tag{7}$$

where R is the reflectance of samples.
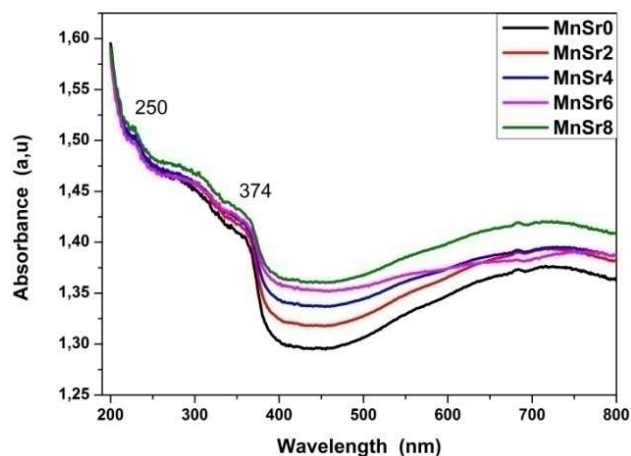
The band gap energy (Eg) was determined using the Tauc
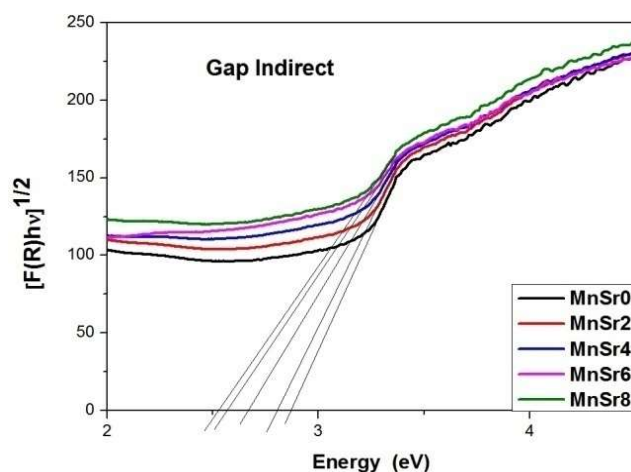
Fig. 6. Absorbance spectra of undoped and Sr-doped α-MnO_2 NWs.

Fig. 7. The Tauc plot used to determine the band gap energy of undoped and Sr-doped α-MnO_2 NWs.

Eq. (8) [5]:

$$(F(R).h\nu)^n = A(h\nu - Eg) \tag{8}$$

where A is a constant, $h\nu$ is the photon energy, and n is equal to ½ or 2 for indirect or direct allowed transitions, respectively.

The intersection of the extrapolation of the linear part of the Tauc plots with the photon energy axis provided the band gap energy (Eg) (Fig. 7). The obtained values of the indirect band gap energy (Table 5) decreased when the Sr-doping

Table 5. Indirect Band Gap Energy and the Urbach Energy of Synthesized α-MnO$_2$ NWs

Sample	Indirect gap (eV)	Urbach energy (meV)
MnSr0	2.87	266.66
MnSr2	2.80	307.69
MnSr4	2.66	363.63
MnSr6	2.57	470.59
MnSr8	2.52	533.33

Fig. 8. PL spectra of undoped and Sr-doped α-MnO$_2$ NWs (excitation at 350 nm).

concentration increased. The slight shift in the band gap energy (E$_g$) toward lower energies was due to the formation of new energy levels in the band gap caused by doping. Similar results have been reported for the Co- and Cu-doped α-MnO$_2$ NPs [28]. Furthermore, the morphology of α-MnO$_2$ with NWs has been shown to have an indirect electronic transition near the band gap of 2.23 eV [35]. Thus, the obtained values of the band gap (Table 5) make it possible to use UV as well as solar radiation to irradiate the synthesized α-MnO$_2$ samples during the photocatalytic process.
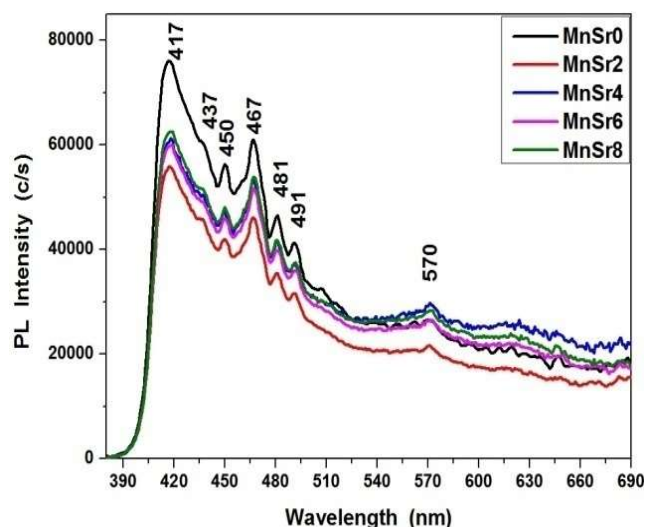
The Urbach energy (EU) is a parameter that reflects the effect of structural disorder caused by Sr-doping on the optical properties of the Sr-doped α-MnO$_2$ samples. EU was determined using the following equation relative to the absorption coefficient (ε) (9) [36]:

$$\ln(\varepsilon) = \ln(\varepsilon_0) + \frac{h\nu}{E_U} \tag{9}$$

where ε0 is a constant related to the material.

For the α-MnO$_2$ samples, the absorption coefficient (ε) was equivalent to F(R). The EU was determined by plotting ln(F(R)) against the hν; then, the inverse of the slope of the linear part of curves gave the EU. The increase in the EU value (Table 5) showed more disorder in the lattice of the doped samples, leading to a change in the optical properties, which, in turn, can influence the photocatalytic process.

Photoluminescence (PL) spectroscopy analysis. PL measurement was used to characterize the charge transfer, photo-generated carriers, and the separation and recombination of the electron-hole pairs. PL spectra (Fig. 8) of the undoped and Sr-doped α-MnO$_2$ NWs were recorded at room temperature and under the excitation wavelength of 350 nm. The observed emission bands were located in the violet-blue-green domain of visible light. The strong violet emission at 417 nm corresponded to the band edge emission signals of well-crystallized α-MnO$_2$ nanocrystals [32]. The blue emission bands at 450, 467, 481, and 491 nm may be assigned to oxygen vacancy-related defects [27,32]. Likewise, a broad and weak green emission at 570 nm can be attributed to both surface dangling bonds and surface defects [32].

Overall, the intensity of emission bands decreased after the Sr-doping due to the formation of new energy levels in the band gap through which excited electrons were relaxed. Since this step increases the lifetime of excited electrons and thus promotes the electron-hole separation, it can enhance the photocatalytic activity.

Catalytic Properties of α-MnO$_2$ NWs

The catalytic properties of undoped and Sr-doped α-MnO$_2$ NWs were studied using an aqueous solution of MB (6 mg l^{-1}) and 0.25 g of α-MnO$_2$ catalyst. The mixture was magnetically stirred in the dark to establish the adsorption/desorption equilibrium of MB molecules on the surface of α-MnO$_2$ NWs. The variation in the concentration of MB dye in the solution was followed by the change in the intensity of the UV-Vis absorbance peak at 664 nm, which

corresponded to the maximum MB absorbance. The absorbance spectra recorded after different stirring time intervals and the evolution of the MB concentration ratio (Ct/C0) are shown in Figs. 9a and 9b, respectively.

The curves show a decrease in the absorbance intensity of MB solution when the time of stirring and the concentration of Sr-doping increased. The changes in the UV-Vis spectra revealed the substantial discoloration of MB dye solution [37].

The adsorption was very fast in the first 2 min (Fig. 10); it reached 49.93% and 99.63% of initial MB concentration for the undoped and MnSr8 samples, respectively. After 2 min, the adsorption slowed down and the adsorption/desorption equilibrium for the undoped sample reached 66.86% after 18 min. The catalytic adsorption of MB was highly improved by the doped sample compared to the undoped sample. After 4 min, the MB dye was almost completely absorbed by the MnSr6 and MnSr8 samples. Similar recent results have been reported for Mn-oxides particles with various sizes and morphologies that were synthesized using different techniques and precursors [38-39]. This high efficiency is mainly due to the increase in the SSA of doped samples, which provide more active sites for the reactant molecules of MB. The high adsorption rate obtained in a very short time makes the synthesized Sr-doped α-MnO$_2$ NWs a potentially effective candidate for practical industrial applications. The mechanism underlying the MB molecule attachment to the surface of α-MnO$_2$ NW catalysts depends on the type of interactions between the adsorbate molecules and the adsorbent binding sites [8,37]. The fast discoloration of MB solution observed during its contact with α-MnO$_2$ NW catalysts can be attributed to the effect of electrostatic interactions, ion exchange, hydrogen bonding, and/or van der Waals forces [40].

Similar absorption behavior has also been reported for the adsorption of organic dyes onto the surface of numerous catalysts [8-10,40]. Studies of such behavior have been conducted against the effect of initial concentration of dye, the mass of catalyst, contact time, agitation speed, crystallinity, structure, morphology, particle size of the catalyst, PH, and the temperature of the aqueous solution [40-42]. On the other hand, to investigate adsorption processes, various kinetic models have been proposed in the literature [4-5,40,43]; these models are classified into adsorption
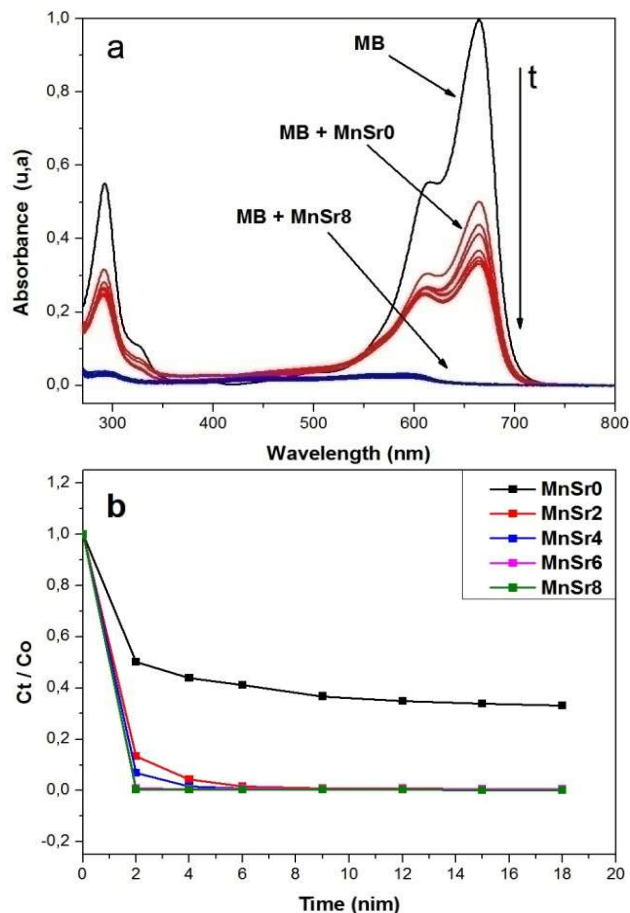

Fig. 9. The catalytic activity of α-MnO$_2$ NWs after different stirring time intervals in the dark: (a) Absorbance spectra of MB solution in the absence and presence of only undoped and MnSr8 samples and (b) Evolution of MB concentration ratio (Ct/C0) for all synthesized samples.
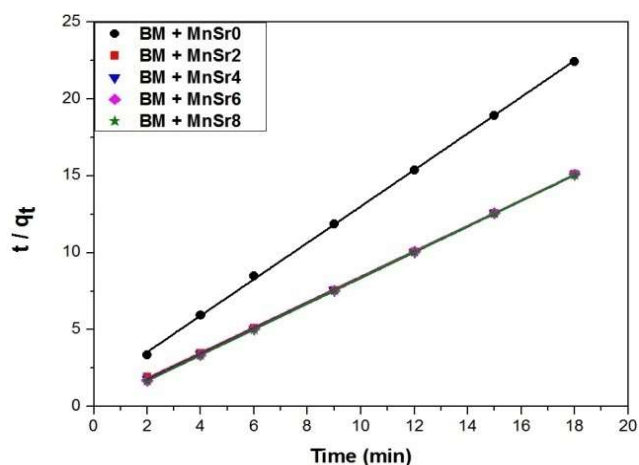

Fig. 10. The plot of t/qt *versus* t and the linear fit.

diffusion and adsorption reaction models. The most frequently used models in this regard are the pseudo-first-order and pseudo-second-order kinetic models, the Elovich model, and the intraparticle diffusion model. It should be noted that each of these models has its own limitations [44].

In this paper, for the adsorption of MB dye by undoped and Sr-doped α-MnO$_2$ NW catalysts, the best results were obtained by applying the pseudo-second-order kinetic model. In this model, it is assumed that adsorption occurs through a chemical reaction, so the adsorption is controlled by the velocity of the chemical reaction. Hence, the adsorption mechanism is chemisorption. The pseudo-second-order kinetic model is expressed as follows [45]:

$$\frac{t}{q_t} = \frac{1}{k_2\, q_e^2} + \frac{t}{q_e} \tag{10}$$

where k_2 (g mg^{-1} min^{-1}) is the pseudo-second-order rate constant, q_t (mg g^{-1}) is the amount of MB adsorbate adsorbed on the surface of α-MnO$_2$ NWs at time t (min), and q_e (mg g^{-1}) is the adsorption capacity at adsorption/desorption equilibrium.

The amount of MB adsorbed at time t (q_t) was calculated by the following Eq. (11) [43]:

$$q_t = \frac{(C_0 - C_t)V}{m} \tag{11}$$

where C_0 (mg l^{-1}) is the initial MB concentration, C_t (mg l^{-1}) is the concentration of MB at time t (min), V (l) is the volume of MB solution, and m (g) is the mass of adsorbent α-MnO$_2$ NWs.

Figure 10 represents the plot of t/q_t *versus* t for the pseudo-second-order model. The linear fit of the plot allowed us to determine k_2 and q_e. The fit of the model was assessed on the basis of the value of the correlation coefficient (R2). An R2 value close to unity indicates a better simulation of experimental data.

As can be seen from Table 6, the values of the correlation coefficient (R2) were very close to unity, indicating that the experimental data fitted well to the pseudo-second-order model. This shows that the adsorption process occurred through chemisorptions. In addition, the values of k_2 indicate that the adsorption of MB molecules sped up when the Sr-doping concentration increased. Likewise, the calculated

Table 6. Pseudo-Second-Order Rate Constants (k_2) Along with the Corresponding Correlation Coefficients (R^2) and the Amounts of MB Adsorbed (q_e) at Equilibrium

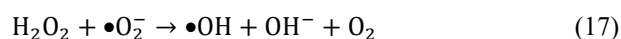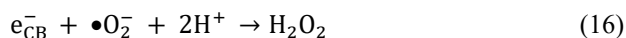| Sample	k_2 (g mg^{-1} min^{-1})	R^2	q_{ecal} (mg g^{-1})	q_{eexp} (mg g^{-1})
MnSr0	1.197	0,9996	0,844	0,802
MnSr2	3.641	0,9998	1,210	1,108
MnSr4	9.543	0,9999	1,199	1,145
MnSr6	134.519	1	1,193	1,149
MnSr8	146.201	1	1,197	1,176

adsorption amounts (qecal) of MB obtained from the pseudo-second-order model (Table 6) were close to the observed experimental adsorption amounts ((qeexp), demonstrating the suitability of the pseudo-second-order kinetic model for the adsorption process. The results of the catalytic adsorption of synthesized Sr-doped α-MnO2 NWs regarding the MB dye were close to that reported in the recent literature [46,47].

Photocatalytic Properties of α-MnO2 NWs

The irradiation of α-MnO$_2$ oxides by suitable light can produce electron-hole pairs, which could be considered as powerful reducing and oxidizing agents, respectively (Eq. (12)) [4].

$$MnO_2 + h\nu \rightarrow e_{CB}^- + h_{VB}^+ \tag{12}$$
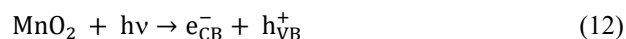
The photo-generated electrons and holes can move to the surface of the α-MnO$_2$ particles and react with the H$_2$O and O$_2$ of the MB solution as follows [4].

$$h_{VB}^+ + H_2O \rightarrow H^+ + \bullet OH \tag{13}$$

$$h_{VB}^+ + OH^- \rightarrow \bullet OH \tag{14}$$

$$e_{CB}^- + O_2 \rightarrow \bullet O_2^- \tag{15}$$

$$e_{CB}^- + \bullet O_2^- + 2H^+ \rightarrow H_2O_2 \tag{16}$$

$$H_2O_2 + \bullet O_2^- \rightarrow \bullet OH + OH^- + O_2 \tag{17}$$

These reactions lead to the formation of •OH radicals, which are powerful oxidants that can mineralize the majority of organic pollutants [5]. To study the photocatalytic activity of synthesized α-MnO$_2$ NWs, the MB solution was subjected to UV irradiation (365 nm) after adsorption/desorption equilibrium in the dark. The recorded absorbance spectra for different irradiation time intervals in the absence and presence of undoped and Sr-doped α-MnO2 NWs are shown in Fig. 11.

It is worth noting that the direct photolysis of MB showed a degradation rate less than 6% after 60 min, which was considered negligible [48] since the photocatalysis process further degrades the MB dye in the presence of catalysts. Figure 12 shows the evolution of the concentration ratio C_t/C_0 of MB dye versus time t (before and after UV irradiation) for α-MnO$_2$ catalysts with different Sr-doping concentrations. It can be observed that for the undoped sample, the photocatalytic degradation of MB increased with the increase in the UV irradiation time, reaching 97.74% in 60 min. However, in the presence of the Sr-doped sample, the photocatalytic process had a minimal effect since almost the entire quantity of MB had been already removed during the catalytic process.

Thus, the doping of α-MnO$_2$ NWs by Sr^{2+} greatly favored the removal of MB dye. A complete and rapid elimination of MB was observed after 4 min of UV irradiation for MnSr6 and MnSr8 samples, which confirms the very high efficacy of these two samples. The observed absorbance bands at 446 and 558 nm (Fig. 11) are related to the formation of intermediate products obtained during the chemisorption of MB [49], and their disappearance under UV irradiation indicates the mineralization stage of MB. Finally, the disappearance of absorbance bands in the ultraviolet range at around 291 and 327 nm, which are specific to MB (Fig. 11), allowed us to conclude that the MnSr8 catalyst was capable of causing the complete mineralization of MB. The mineralization of MB can occur according to the following reaction [42]:

$$\text{MBdye} + \bullet\text{OH} \rightarrow H_2O + CO_2 + \text{mineralization products} \qquad (18)$$
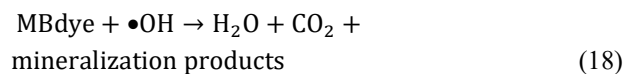
In Table 7, for the sake of comparison, some results on the degradation are grouped with the α-MnO$_2$ of certain
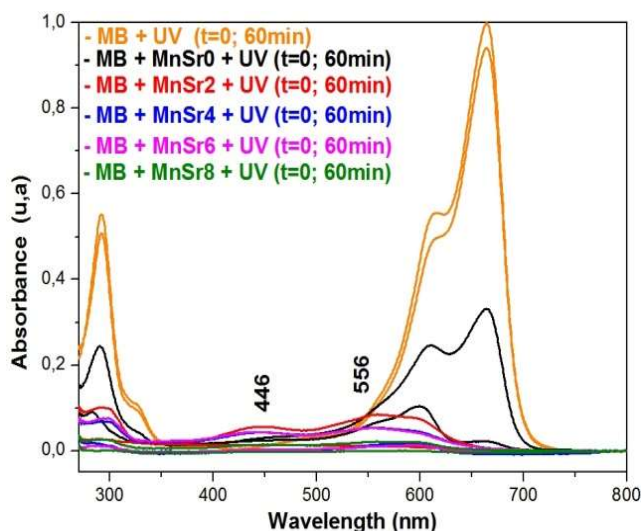

Fig. 11. Absorbance spectra of MB solution in the absence and presence of undoped and Sr-doped α-MnO$_2$ NWs under UV irradiation (365 nm) at t = 0 and t = 60 min, which are the initial and final time of photocatalysis degradation, respectively.
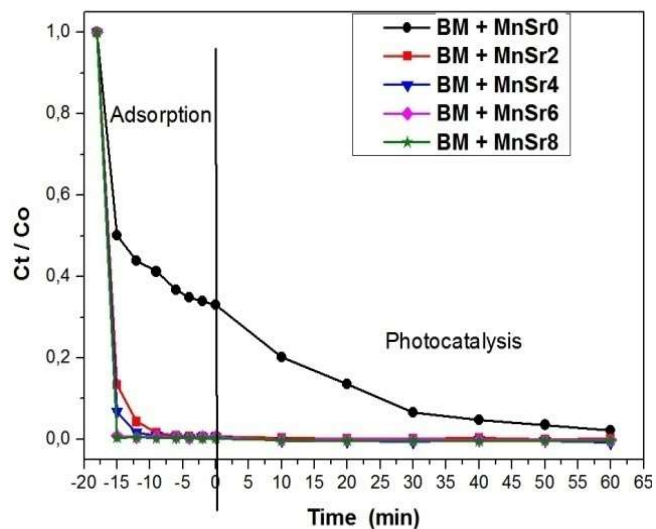

Fig. 12. Concentration ratios (C_t/C_0) of MB dye *versus* time t (before and after UV irradiation).

organic dyes. It is clear that the α-MnO$_2$ photocatalyst was highly efficient in the degradation of both cationic and anionic dyes. In some cases, the degradation is nearly complete within a short time of 10 min [2,50]; however, this is infrequent when many other photocatalysts are used.

Table 7. A Comparison of Degradation Rates for Some Organic Dyes by the α-MnO$_2$ Photocatalyst

Dye	Degradation rate (%)	Irradiation Time (min)	Ref.
Rhodamine B	99.99	10	[2]
Rhodamine-6G	95.64	10	[2]
Congo red	97.14	10	[2]
Methyl blue	96.39	10	[2]
Methyl orange	99.96	10	[2]
Methylene blue	91.1	30	[51]
Methyl orange	89,8	120	[51]
Methylene blue	98	10	[50]
Methylene blue	100	4	This work

CONCLUSIONS

In summary, undoped and Sr-doped α-MnO$_2$ NWs were successfully synthesized *via* a simple hydrothermal method. The obtained NWs had a length of up to 5.91 μm and a cross-section of the nanometric scale. The structural investigation of Sr-doped α-MnO$_2$ NWs revealed that the Sr-dopant was housed in large tunnels along the c-axis of the tetragonal structure of α-MnO$_2$. The increase in the Sr-dopant concentration led to a reduction in the length of NWs, a wider cross-section, and an increase in the SSA of the particles. The optical characterization demonstrated a slight reduction in the band gap energy owing to the localized new energy levels in the band gap caused by the Sr-doping. Furthermore, the photoluminescence bands observed in the visible range can be assigned to oxygen vacancy-related defects. The undoped α-MnO$_2$ NWs showed significant catalytic and photocatalytic activities; however, the Sr-doped α-MnO$_2$ NWs exhibited a strong catalytic activity. The larger SSA of the MnSr8 sample acted as a favorable factor and led to the almost complete adsorption of the MB dye in a very short time (4 min) during the catalytic process. The easy preparation of Sr-doped α-MnO$_2$ NWs catalysts and their high efficiency in the elimination of organic pollutant MB make them a promising potential candidate for practical use in environmental protection technologies.

REFERENCES

[1] Boulkroune, R.; Sebais, M.; Messai, Y.; Bourzami, R.; Schmutz, M.; Blanck, C.; Halimi, O.; Boudine, B., Hydrothermal synthesis of Strontium-doped ZnS nanoparticles: structural, electronic and photocatalytic investigations. *BMS* **2019**, *42*, 223, https://doi.org/10.1007/s12034-019-1902-2.

[2] Baral, A.; Das, D. P.; Minakshi, M.; Ghosh, M. K.; Padhi, D. K., Probing Environmental Remediation of RhB Organic Dye Using α-MnO$_2$ under Visible-Light Irradiation: Structural, Photocatalytic and Mineralization Studies. *CS* **2016**, *1* (14), 4277-4285.

[3] Xiao, L.; Sun, W.; Zhou, X.; Cai, Z.; Hu, F., Facile synthesis of mesoporous MnO$_2$ nanosheet and microflower with efficient photocatalytic activities for organic dyes. *V* **2018**, *156*, 291-297, https://doi.org/10.1016/j.vacuum.2018.07.045

[4] Haya, S.; Brahmia, O.; Halimi, O.; Sebais, M.; Boudine, B., Sol-gel synthesis of Sr-doped SnO$_2$ thin films and their photocatalytic properties. *MR* **2017**, *4* (10), https://doi.org/10.1088/2053-1591/aa8deb.

[5] Ayadi, M.; Benhaoua, O.; Sebais, M.; Halimi, O.; Boudine, B.; Aida, M. S., Effect of cerium doping on the structural, optical and photocatalytic properties of SnO$_2$ thin films prepared by spray pyrolysis method. *MRE* **2019**, *6* (7), 076407, https://doi.org/10.1088/2053-1591/ab10c5.

[6] Shahmoradi, B.; Negahdary, M.; Maleki,A., Hydrothermal Synthesis of Surface-Modified, Manganese-Doped TiO$_2$ Nanoparticles for Photodegradation of Methylene Blue. *EES* **2012**, *29* (11), 1032, https://doi.org/10.1089/ees.2011.0519.

[7] Zhou, X.; Shi, T.; Zhou, H., Hydrothermal preparation of ZnO-reduced graphene oxide hybrid with high performance in photocatalytic degradation. *ASS* **2012**, *258* (17), 6204-6211, https://doi.org/10.1016/j.apsusc.2012.02.131.

[8] Zhao, G.; Li, J.; Ren, X.; Hu, J.; Huc, W.; Wang, X., Highly active MnO$_2$ nanosheet synthesis from graphene oxide templates and their application in efficient oxidative degradation of methylene blue. *RSCA* **2013**, *3* (31), 12909-12914, https://doi.org/10.1039/c3ra40942b.

[9] Zhang, Y. X.; Guo, X. L.; Huang, M.; Hao, X. D.; Yuan, Y.; Hua, C., Engineering birnessite-type MnO_2 nanosheets on fiberglass for pH-Dependent Degradation of Methylene Blue. *JPCS* **2015**, *83*,40-46, http://dx.doi.org/10.1016/j.jpcs.2015.03.015.

[10] Sun, M.; Lin, T.; Cheng, G.; Ye, F.; Yu, L., Hydrothermal Synthesis of Boron-Doped MnO_2 and Its Decolorization Performance. *JN* **2014**, 150-156, http://dx.doi.org/10.1155/2014/175924.

[11] Wei, M.; Konishi, Y.; Zhou, H.; Sugihara, H.; Arakawa, H., Synthesis of single-crystal manganese dioxide nanowires by a soft chemical process. *N* **2005**, *16* (2), 245-249, https://doi.org/10.1088/0957-4484/16/2/011.

[12] Lou, X. W. D.; Archer, L. A.; Yang, Z., Hollow Micro-/Nanostructures: Synthesis and Applications. *AM* **2008**, *20* (21), 3987-4019, https://doi.org/10.1002/adma.200800854.

[13] Li, Y.; Wang, J.; Zhang, Y.; Banis, M. N.; Liu, J.; Geng, D.; Li, R.; Sun, X., Facile controlled synthesis and growth mechanisms of flower-like and tubular MnO_2 nanostructures by microwave-assisted hydrothermal method. *CIS* **2012**, *369* (1), 123-128, https://doi.org/10.1016/j.jcis.2011.12.013.

[14] Wang, Y.; Indrawirawan, S.; Duan, X.; Sun, H.; Ang, H. M.; Tadé, M. O.; Wang, S., New insights into heterogeneous generation and evolution processes of sulfate radicals for phenol degradation over one-dimensional α-MnO_2 nanostructures. *CE* **2015**, *266*, 12-20, https://doi.org/10.1016/j.cej.2014.12.066.

[15] Yang, Z.; Ford, D. C.; Park, J. S.; Ren, Y.; Kim, S.; Kim, H.; Fister, T. T.; Chan, M. K. Y.; Thackeray, M. M., Probing the Release and Uptake of Water in α-MnO_2·xH_2O. *CM* **2017**, *29* (4) 1507-1517, https://doi.org/10.1021/acs.chemmater.6b03721.

[16] John, R. E.; Chandran, A.; Thomas, M.; Jose, J.; George,K. C., Surface-defect induced modifications in the optical properties of α-MnO_2nanorods. *ASS* **2016**, *367*, 43-51, https://doi.org/10.1016/j.apsusc.2016.01.153.

[17] Reenu, E. J.; Anoup, C.; Justin, G.; Ajai, J.; Gijo, J.; Joshy, J.; Unnikrishnan, N. V.; Marykutty, T.; George, K. C., High temperature ferroelectric behaviour in α-MnO_2 nanorodsrealised through enriched oxygen vacancy induced non-stoichiometry. *PCCP*

2017, *19* (42), 28756-28771, https://doi.org/10.1039/C7CP05724E.

[18] Liu, W. X.; Zhu, X. L.; Liu, S. Q.; Gu, Q. Q.; Meng, Z. D., Near-Infrared-Driven Selective Photocatalytic Removal of Ammonia Based on Valence Band Recognition of an α-MnO_2/N-Doped Graphene Hybrid *CACSO* **2018**, *3* (5), 5537-5546, https://doi.org/10.1021/acsomega.8b00161.

[19] Zhang, D.; Luo, R., Modifying the BET model for accurately determining specific surface area and surface energy components of aggregates. *CBM* **2018**, *175*, 653-663, https://doi.org/10.1016/j.conbuildmat.2018.04.215.

[20] Ren, Q.; Ding, L.; Dai, X.; Jiang, Z.; Ye, G.; Schutter, G. D., Determination of specific surface area of irregular aggregate by random sectioning and its comparison with conventional methods. *CBM* **2021**, *273*, 122019, https://doi.org/10.1016/j.conbuildmat.2020.122019.

[21] Zhang,C.; Lu,N., Augmented Brunauer Emmett-Teller Equation for Water Adsorption on Soils. *VZJ* **2019**, *18* (1), 1-12, https://doi.org/10.2136/vzj2019.01.0011.

[22] Jeong, H. Y.; Lee, J. H.; Hayes, K. F., Characterization of synthetic: Crystal structure, particle size, and specific surface area. *GCA* **2008**, *72* (2), 493-505, https://doi:10.1016/j.gca.2007.11.008.

[23] Gao, T.; Fjellvåg, H.; Norby, P., A comparison study on Raman scattering properties of α- and β-MnO_2.*ACA* **2009**, *648* (2), 235-239, https://doi.org/10.1016/j.aca.2009.06.059.

[24] Ashwani, K.; Amit, S.; Arvind, K.; Yogesh, K.; Ramesh, C., An efficient α-MnO_2nanorods forests electrode for electrochemical capacitors with neutral aqueous electrolytes. *EA* **2016**, *220*, 712-720, http://dx.doi.org/10.1016/j.electacta.2016.10.168.

[25] Mo, L.; Zheng, H., Growth of MnO_2 nanoflakes on TiO_2 nanorods for pseudocapacitor. *JAC* **2019**, *788*, 1162-1168, https://doi.org/10.1016/j.jallcom.2019.02.321.

[26] Rout, K.; Mohapatra, M.; Anand, S., Acritical analysis of cation adsorption from single and binary solutions on low surface area β-MnO_2. *ASS* **2013**, *270*, 205-218, https://doi.org/10.1016/j.apsusc.2013.01.002.

[27] Toufiq, A. M.; Wang, F.; Shah, H. U., Synthesis and Characterization of MnO_2 Nanowires: Lattice

Vibrations and Photoluminescence Properties. *PSSC* **2017**, *14* (10), 1700176, https://doi.org/10.1002/pssc.201700176.

[28] Mondal, D.; Paul, B. K.; Das, S.; Bhattacharya, D.; Ghoshal, D.; Nandy, P.; Das, K.; Das, S., Synthesis and Property of Copper-Impregnated α-MnO_2 Semiconductor Quantum Dots. *L* **2018**, *34* (43), 12702-12712, https://doi.org/10.1021/acs.langmuir.8b01745.

[29] Chen, D.; Ding, D.; Li, X.; Waller, G.; Xiong, X.; El-Sayed, M.; Liu, M., Probing the Charge Storage Mechanism of a Pseudo capacitive MnO_2 Electrode Using in Operando Raman Spectroscopy. *CM* **2015**, *27* (19), 6608-6619, https://doi.org/10.1021/acs.chemmater.5b03118.

[30] Maiti, S.; Pramanik, A.; Mahanty, S., Interconnected Network of MnO_2 Nanowires with a 'Cocoonlike' Morphology: Redox Couple-Mediated Performance Enhancement in Symmetric Aqueous Supercapacitor. *ACSAMI* **2014**, *6* (13), 10754-10762, https://doi.org/10.1021/am502638d.

[31] Mylarappa, M.; Venkata, V. L.; Vishnu, M. K. R.; Nagaswarupa, H. P.; Raghavendra, N., A facile hydrothermal recovery of nano sealed MnO_2 particle from waste batteries: An advanced material for electrochemical and environmental applications. *MSE* **2016**, *149* (1), 012178, https://doi:10.1088/1757-899X/149/1/012178.

[32] Toufiq, A. M.; Wang, F.; Javed, Q.; Li, Q.; Li, Y., Hydrothermal synthesis of MnO_2 nanowires: structural characterizations, optical and magnetic properties. *APA* **2014**, *116*, 1127-1132, https://doi.org/10.1007/s00339-013-8195-0.

[33] Liu, W. X.; Zhu, X. L.; Liu, S. Q.; Gu, Q. Q.; Meng, Z. D., Near-Infrared-Driven Selective Photocatalytic Removal of Ammonia Based on Valence Band Recognition of an α-MnO_2/N-Doped Graphene Hybrid Catalyst. *ACSO* **2018**, *3* (5), 5537-5546, https://doi:10.1021/acsomega.8b00161.

[34] Ahmed, S.; Khan, Z. H.; Rafat, M., Studies on MnO_2 Nanorods and Their Application for Supercapacitor. *CN* **2017**, *2* (1), 45-52, https://doi:10.2174/2405461502666170405170331.

[35] Sakai, N.; Ebina, Y.; Takada, K.; Sasaki, T., Photocurrent generation from semiconducting manganese oxide nanosheets in response to visible light. *JPCB* **2005**, *109* (19), 9651-9655, https://doi.org/10.1021/jp0500485.

[36] Somvanshi, A.; Manzoor, S.; Husain, S.; Khan, M. W., Exploration of Electronic Structure, Vibrational Spectra and Defect Energy of Mn Incorporated Neodymium Orthoferrite Perovskites. *AIPCP* **2019**, *2115*, 030073, https://doi.org/10.1063/1.5112912.

[37] Dhanasekaran, T.; Padmanaban, A.; Gnanamoorthy, G.; Manigandan, R.; Kumar, S. P.; Munusamy, S.; Stephen, A.; Narayanan, V., Preparation and Optical Studies of Layered Double Hydroxides for Photo Catalytic Degradation of Organic Dyes. Mechanics, *MSE* **2017**, *9* (1), 70-71, https://doi:10.2412/mmse.97.8.19.

[38] Rajrana, K.; Gupta, A.; Rameez Ahmad Mir, R, A.; Pandey, O. P., Facile sono-chemical synthesis of nanocrystalline MnO_2 for catalytic and capacitive applications. *Phys. B: Condens. Matter.* **2019**, *564*, 179-185, https://doi.org/10.1016/j.physb.2019.04.002.

[39] Li, J.; Zhou, L.; Song, Y.; Yu, X.; Li, X.; Liu, Y.; Zhang, Z.; Yuan, Y.; Yan, S.; Zhang, J., Green fabrication of porous microspheres containing cellulose nanocrystal/MnO_2 nanohybrid for efficient dye removal. *Carbohydr. Polym.* **2021**, *270*, 118340, https://doi.org/10.1016/j.carbpol.2021.118340.

[40] Mittal, H.; Alhassan, S. M.; Ray, S. S., Efficient organic dye removal from wastewater by magnetic carbonaceous adsorbent prepared from corn starch. *JECE* **2018**, *6* (6), 7119-713, https://doi.org/10.1016/j.jece.2018.11.010.

[41] Junghum, H.; Jun, B. M.; Heo, J.; Lee, G.; Yoon, Y.; Park, C. M., Highly efficient organic dye removal from waters by magnetically recoverable $La_2O_2CO_3$/$ZnFe_2O_4$-reduced graphene oxide nanohybrid. *CI* **2019**, *45* (15), 19247-19256, https://doi.org/10.1016/j.ceramint.2019.06.173.

[42] Wei, W.; Yang, L.; Zhong, W. H.; Li, S. Y.; Cui, J.; Wei, Z. G., Fast Removal of Methylene Blue From Aqueous Solution By Adsorption Onto Poorly Crystalline Hydroxyapatite Nanoparticles. *DJNB* **2015**, *10* (4), 1343-1363.

[43] Al-Ghouti, M. A.; Khraisheh, M. A. M.; Ahmad, M. N. M.; Allen, S., Adsorption behaviour of methylene blue onto Jordanian diatomite: A kinetic study.

JHM **2009**, *165* (1,3), 589-598, https://doi.org/10.1016/j.jhazmat.2008.10.018.

[44] Abdullah, T. A.; Rasheed, R. T.; Juzsakova, T.; Al-Jammal, N.; Mallah, M. A.; Cuong, L. P.; Salman, A. D.; Domokos, E.; Ali, Z.; Cretescu, I., Preparation and characterization of MnO_2-based nanoparticles at different annealing temperatures and their application in dye removal from water. *Int. J. Environ. Sci. Technol.* **2021**, *18*, 1499-1512, https://doi.org/10.1007/s13762-020-02956-x.

[45] Hui, M.; Shengyan, P.; Yaqi, H.; Rongxin, Z.; Anatoly, Z.; Wei, C., A Highly Efficient Magnetic Chitosan "Fluid" Adsorbent with a High Capacity & Fast Adsorption Kinetics for Dyeing Wastewater Purification. *CEJ* **2018**, *345*, 556-565, https://doi.org/10.1016/j.cej.2018.03.115.

[46] Salari, H.; Kohantorabi, M., Heterogeneous photocatalytic degradation of organic pollutant in aqueous solutions by S-scheme heterojunction in nickel molybdate nanocomposites. *J. Environ. Chem. Eng.* **2021**, *9*, 105903, https://doi.org/10.1016/j.jece.2021.105903.

[47] Tran, H. N.; You, S. J.; Bandegharaei, A. H.; Chao, H. P., Mistakes and inconsistencies regarding adsorption of contaminants from aqueoussolutions: A critical

review. *WR* **2017**, *120* (1), 88-116, https://doi.org/10.1016/j.watres.2017.04.014.

[48] Ding, W.; Zhao, L.; Yan, H.; Wang, X.; Liu, X.; Zhang, X.; Huang, X.; Hang, R.; Wang, Y.; Yao, X.; Tang, B., Bovine serum albumin assisted synthesis of Ag/Ag$_2$O/ZnO photocatalyst with enhanced photocatalytic activity under visible light. *CSAPEA* **2019**, *568*, 131-140, https://doi.org/10.1016/j.colsurfa.2019.02.015.

[49] Zhang, H.; Lin, C.; Han, T.; Du, F.; Zhao, Y.; Li, X.; Sun, Y., Visualization of the formation and 3D porous structure of Ag doped MnO2 aerogel monoliths with high photocatalytic activity. *ACSSCE* **2016**, *4* (12), 6277-6287, https://doi.org/10.1021/acssuschemeng.6b00578.

[50] Balakumar, V.; Ryu, J. W.; Kim, H.; Manivannan, R.; Son, Y. A., Ultrasonicsynthesis of α-MnO$_2$ nanorods: An efficient catalytic conversion of refractorypollutant, methylene blue. *US* **2020**, *62*, 104870, https://doi.org/10.1016/j.ultsonch.2019.104870.

[51] Zhao, T.; Duan, F.; Jiang, X.; Xu, H.; Gao, X.; Wang, J., Hydrothermal Synthesis of Three Structured MnO_2 Nanomaterials and Their Performance for Catalytic Oxidation of Resorcinol and Formaldehyde. *CL* **2016**, *45* (4), 457-459, https://doi.org/10.1246/cl.160072.